Research on Input-Parallel Single-Switch Wireless Power Transfer System With Constant-Current and Constant-Voltage Output

Quanlei Zhang, *Student Member, IEEE*, Chunfang Wang, *Member, IEEE*, Hao Yuan, *Student Member, IEEE*, Shuo Zhang, *Student Member, IEEE*, Jingyu Wang, *Student Member, IEEE*, Dongxue Li, *Student Member, IEEE*, and Lingyun Yang

***Abstract*—The full-bridge can further improve the output power through parallel inverters. The inverter output voltage of single-switch *LC*-resonant circuit is a combination of trapezoidal wave and half-sine wave; there is no relevant research on parallel connection of single-switch *LC*-resonant circuit. Therefore, this article presents a novel input-parallel single-switch *LC*-resonant circuit; this topology adopts switchable secondary networks for constant-current (CC) and constant-voltage (CV) output, and prevents shoot-through of power switches. The decoupling between transmitters simplifies the analysis and calculation. The input-parallel structure avoids the unbalanced input voltage of each inverter and improves the stability of the wireless power transfer system. CC and CV output modes can be achieved by controlling one relay without adding dc–dc converters or changing the switching frequency. This article includes decoupling equivalent analysis of coils, topologies analysis of CC mode and CV mode, calculation of equivalent input ac voltage source, design of magnetic coupler, and circuit parameters. Finally, a 1-kW experimental prototype is built to verify the theoretical analysis; the maximum efficiency can reach up to 92.5%.**

***Index Terms*—Constant-current (CC), constant-voltage (CV), input-parallel, single-switch, wireless power transfer (WPT).**

I. INTRODUCTION

WITH THE development of wireless power transfer (WPT), this technology is gradually coming into people's vision. The WPT technology has the advantages of safety, reliability, and convenience [1], [2], which can be used in different applications. For example, there are wireless charging for electric vehicles [3]–[8], drones [9], [10], and implanted biomedical devices [11]–[13]. In the WPT system, the topologies are mainly divided into full-bridge inverter, half-bridge inverter, and bridgeless inverter topologies. The bridgeless inverter topologies [14]–[21], such as Class-E inverter, Class EF (or E/F) inverter, and single-switch *LC*-resonant circuit, have emerged. The topology of single-switch *LC*-resonant circuit is shown in Fig. 1. Compared with the full-bridge circuit and half-bridge circuit [22]–[25], the single-switch *LC*-resonant circuit avoids shoot-through of power switches, and the reliability of the WPT system is improved.

In order to provide high and extendable power levels for WPT system, the inverters can be in parallel [26]–[28] or in series [29]. Each inverter structure has the same input dc voltage through parallel connection, and the output power is increased by increasing the output current of inverters. For the series inverters structure in [29], the output power can be increased by increasing the input voltage, in order to achieve input voltage sharing, the dividing capacitor suppression, and duty cycle adjustment are adopted. However, the unbalanced input voltage of each inverter module increases the complexity of system analysis. At present, the parallel or series structure of inverters is mostly based on full-bridge; the full-bridge circuit has the risk of shoot-through problem, which reduces the stability of the WPT system.

Increasing output power by parallel cascading single-switch *LC* circuits is proposed in this article. In addition, according to the coils structure in the WPT system, the circuits with multiple transmitting coils [30], [31] or multiple receiving coils [32]–[34] can be divided into two types, one is decoupling among coils, the other is coupling among coils. The multiple transmitters corresponding to a single receiver have higher efficiency than the single transmitter corresponding to a single receiver [35], [36]. In [31], a method of data-driven modeling for a class of multiple-transmitter single-receiver WPT system is proposed; the cross-couplings among the transmitting coils make the analysis and design more complex. The mutual decoupling of the coils can reduce the complexity of analysis [37]–[39]. The double-D quadrature pad or bipolar pad (BP) can realize the magnetic decoupling. The BP coil is composed of two identical and partially overlapped coils; the decoupling is realized by adjusting the overlapping position. In [40], the maximum efficiency is achieved by controlling the equivalent impedance of the BP coil to be the same, and the ability of misalignment tolerance is improved. The core of WPT system is the magnetic coupler; there will be inevitable misalignment between the transmitting coil and the receiving coil; it is very important for magnetic coupler to have high misalignment tolerance ability [41]–[43].

Manuscript received June 9, 2021; revised August 23, 2021; accepted September 23, 2021. Date of publication October 7, 2021; date of current version December 31, 2021. This work was supported in part by the National Natural Science Foundation of China under Grant 51877113. Recommended for publication by Associate Editor J. Acero. (*Corresponding author: Chunfang Wang*.)

The authors are with the School of Electrical Engineering, Qingdao University, Qingdao 266071, China (e-mail: 2019026083@qdu.edu.cn; qduwcf@qdu.edu.cn; 2019026080@qdu.edu.cn; 2019020701@qdu.edu.cn; 2019020696@qdu.edu.cn; 2019026062@qdu.edu.cn; qduyly@163.com).

Color versions of one or more figures in this article are available at https://doi.org/10.1109/TPEL.2021.3118434.

Digital Object Identifier 10.1109/TPEL.2021.3118434

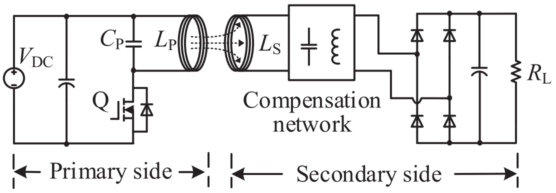

Fig. 1. Topology of single-switch *LC*-resonant circuit.

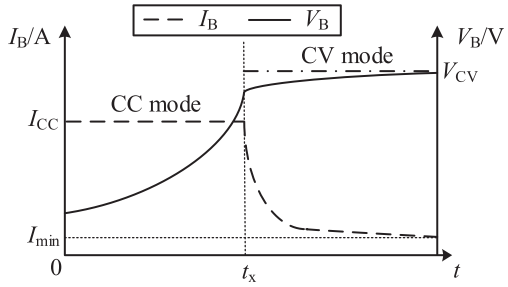

Fig. 2. CC and CV charging curves of a lithium-ion battery.

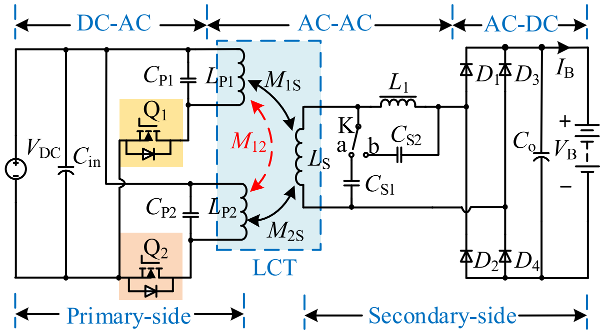

Fig. 3. Proposed input-parallel topology based on single-switch *LC*-resonant circuit.

This article proposes an input-parallel structure based on the single-switch *LC*-resonant circuit, which can improve the output power, and avoid shoot-through of power switches in this topology. In addition, the battery charging generally adopts constant-current (CC) charging and constant-voltage (CV) charging [44], [45]. In order to achieve CC output and CV output, there are generally three methods. The first method is to add dc/dc converter behind the secondary-side rectifier; the CC output and CV output are controlled [46], [47]. The second method is to change the switching frequency of MOSFETs in the inverter bridge; the double-sided *LCC* compensation network is proposed in [48]; the CV/CC output can be realized by changing the switching frequency without changing the circuit parameters; and this topology is suitable for wireless charging of batteries. In the single-switch circuit, P-*CLCL* compensation network and frequency modulation control are used to achieve high-precision CC output and CV output [49]. The third method is to control the working state of MOSFETs or relays; such switching hybrid topologies were studied to achieve CC output and CV output [50]–[52]. In order to reduce the cost of the circuit and keep the resonant frequency unchanged, this article proposes a method to realize CC and CV output by switching the compensation network only at the secondary side in the proposed input-parallel topology based on single-switch *LC*-resonant circuit.

The CC and CV charging curves of a lithium-ion battery are shown in Fig. 2, the I_{CC} is the charging current in CC mode, the V_{CV} is the charging voltage in CV mode, and the I_{min} is the cut-off charging current. I_B is the variation trend of the battery current, and V_B is the variation trend of the battery voltage.

As shown in Fig. 3, it is the proposed input-parallel topology based on single-switch *LC*-resonant circuit. Compared with the traditional single-switch *LC*-resonant circuit, the novel topology can make the output power larger. In this article, the BP pad is selected as the transmitters and the rectangular coil is used as the receiver. The BP pad consists of two identical partially overlapped coils that are mutually decoupled; the cross-coupling between the transmitters would be small enough to be ignored. Besides, the analysis and calculation of the WPT system are simplified. The compensation networks can be switched through the relay to achieve CC output or CV output, and the control method of CC and CV is simpler than the method of changing the switching frequency of MOSFETs.

The rest of this article is organized as follows. The decoupling equivalent model of primary coils and secondary coil is analyzed, and the compensation networks of CC mode and CV mode are analyzed in Section II. In Section III, the equivalent input ac voltage is calculated theoretically, zero-voltage switching (ZVS) margin is designed, and then the CC and CV gain curves and the sensitivity of circuit parameters are analyzed. In Section IV, the magnetic coupler and circuit parameters are designed. A 1-kW experimental prototype is built to verify the theoretical analysis in Section V. The output current is 6.5 A in CC mode, and the output voltage is 155 V in CV mode; the output characteristics of CC mode and CV mode are analyzed, respectively. Finally, Section VI concludes this article.

II. Analysis Principle and Compensation Network

The proposed input-parallel topology based on single-switch *LC*-resonant circuit is shown in Fig. 3. The primary side can be regarded as two identical traditional single-switch *LC*-resonant circuits in parallel. Q_1 and Q_2 are power MOSFETs in their respective single-switch *LC*-resonant circuit. C_{P1} and C_{P2} are the capacitances of the compensated capacitors. LCT is loosely coupled transformer, and L_{P1} and L_{P2} are the self-inductance of the transmitting coils, which are partially overlapped to form the BP coil. L_S is the self-inductance of the receiving coil, the secondary side is *LCL*/S compensation networks, C_{S1} and C_{S2} are capacitances of the compensated capacitors, and L_1 is the inductance of the Sendust core inductor. K is the single-pole double-throw (SPDT) relay, and K is used to switch different compensation networks for CC and CV output. Logic control of SPDT relay is shown in Fig. 4; "a" and "b" are normally closed contact and open contact of SPDT relay. When the relay K and capacitor C_{S1} are connected, the secondary side can be regarded as *LCL* compensation network, and the circuit works in CC mode. When the relay K and capacitor C_{S2} are connected, the secondary side can be regarded as S-compensation network, and the circuit works in CV mode.

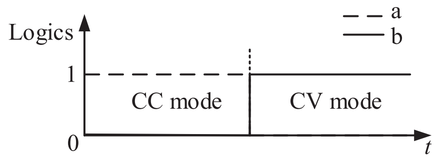

Fig. 4. Logic control of SPDT relay.

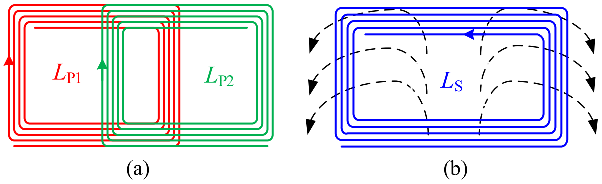

(a)

(b)

Fig. 5. Coil structure. (a) Transmitting coils. (b) Receiving coil.

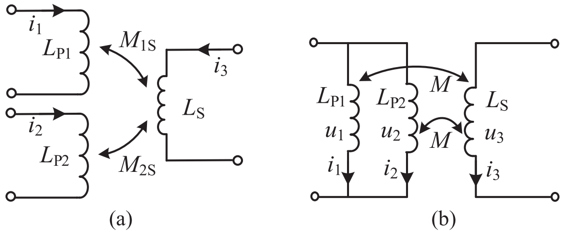

(a)

(b)

Fig. 6. Equivalent analysis between the transmitters and the receiver.

A. Decoupling Equivalent Analysis of Coils

For the proposed input-parallel topology based on single-switch *LC*-resonant circuit, in order to get the accurate resonance relationship among the components, it is necessary to analyze the decoupling equivalent model between the transmitting coils and the receiving coil. The coil structure is shown in Fig. 5.

The equivalent analysis between the transmitting coils and the receiving coil is shown in Fig. 6. As shown in Fig. 6(a), M_{iS} is the mutual inductance between L_{Pi} and L_S $(i = 1, 2)$; the mutual inductance between the transmitting coils would be small enough to be ignored ($M_{12} = 0$). Since the primary-side circuits are in parallel structure, when the switching frequencies of two MOSFETs are the same, the input voltages of the two compensation networks would be equal. The BP pad consists of two identical and partially overlapped coils, when the mutual inductances between the transmitters and receiver are assumed to be identical, $M = M_{1S} = M_{2S}$; Fig. 6(a) can be simplified as shown in Fig. 6(b). In Fig. 6(b), the variables u_1, u_2, and u_3 are the coils voltages of L_{P1}, L_{P2}, and L_S. i_1, i_2, and i_3 are the coils currents of L_{P1}, L_{P2}, and L_S, respectively.

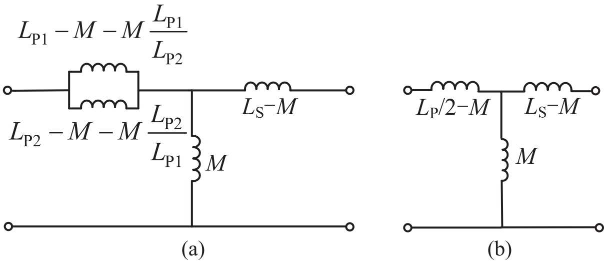

(a)

(b)

Fig. 7. T-type equivalent network.

According to Kirchhoff's voltage law (KVL), the matrix equation in Fig. 6(b) can be obtained as follows:

$$\begin{bmatrix} j\omega L_{P1} & 0 & j\omega M \\ 0 & j\omega L_{P2} & j\omega M \\ j\omega M & j\omega M & j\omega L_S \end{bmatrix} \cdot \begin{bmatrix} i_1 \\ i_2 \\ i_3 \end{bmatrix} = \begin{bmatrix} u_1 \\ u_2 \\ u_3 \end{bmatrix} \tag{1}$$

u_3 can be expressed as follows:

$$u_3 = j\omega\,(L_S - M)\,i_3 + j\omega M\,(i_1 + i_2 + i_3)\,. \tag{2}$$

Since $u_1 = u_2$, $L_{P1}i_1 = L_{P2}i_2$, and i_1 and i_2 can be expressed as $i_2 = \frac{L_{P1}}{L_{P2}}i_1$ or $i_1 = \frac{L_{P2}}{L_{P1}}i_2$, the relational expressions between the current and voltage can be derived as shown in (3) at the bottom of this page.

According to the relationship among u_1, u_2, and u_3 in (3), T-type equivalent network is shown in Fig. 7. The decoupling equivalent model is shown in Fig. 7(a). Since the BP pad is composed of two identical and partially overlapped coils, $L_P = L_{P1} = L_{P2}$, Fig. 7(a) is equivalent to Fig. 7(b). The equivalent network in Fig. 7(b) provides the basis for the analysis of the compensation networks.

B. Analysis of CC Mode and CV Mode

In this article, the relay K in the secondary side is used to switch the compensation networks for CC output and CV output, respectively. When the proposed WPT system works in CC mode, the relay K and resonant capacitor C_{S1} are connected, and the resonant capacitor C_{S2} is in open-circuit state. The equivalent model in CC mode is shown in Fig. 8; the output ac equivalent resistance is defined as R_{eq}. By applying Thévenin's and Norton's theorems, the structure of Fig. 8(a) can be simplified as shown in Fig. 8(c). When the circuit works in the CV mode, the relay K and resonant capacitor C_{S2} are connected, and the resonant capacitor C_{S1} is in the open-circuit state. The equivalent model in CV mode is shown in Fig. 9. As shown in Fig. 9(a), when the value of C_{S2} is sufficiently large, the parallel connection of L_1 and C_{S2} can be regarded as an equivalent capacitance C'. Finally, the structure of Fig. 9(a) can be simplified as shown in Fig. 9(c).

$$\begin{bmatrix} j\omega\left(L_{P1} - M - M\frac{L_{P1}}{L_{P2}}\right) & 0 & 0 & j\omega M \\ 0 & j\omega\left(L_{P2} - M - M\frac{L_{P2}}{L_{P1}}\right) & 0 & j\omega M \\ 0 & 0 & j\omega\,(L_S - M) & j\omega M \end{bmatrix} \cdot \begin{bmatrix} i_1 \\ i_2 \\ i_3 \\ i_1 + i_2 + i_3 \end{bmatrix} = \begin{bmatrix} u_1 \\ u_2 \\ u_3 \end{bmatrix} \tag{3}$$

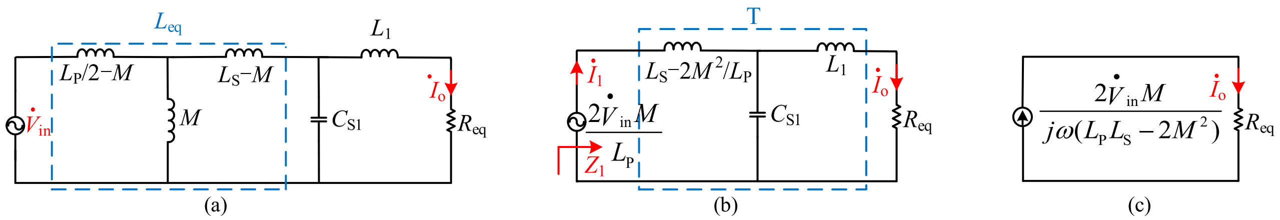

Fig. 8. Equivalent model in CC mode.

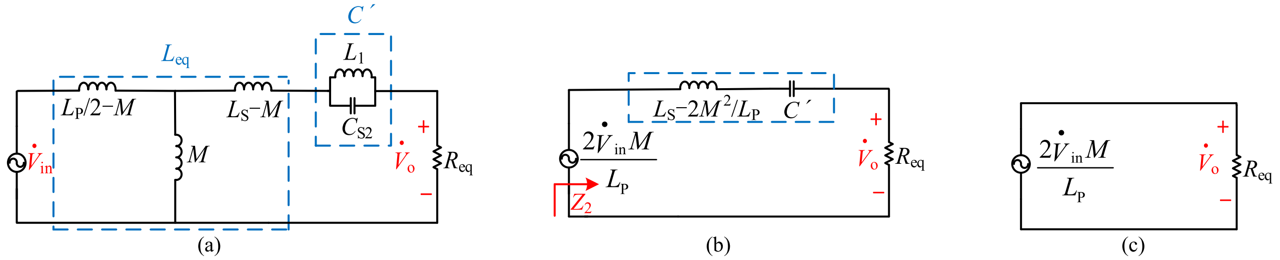

Fig. 9. Equivalent model in CV mode.

For the convenience of illustration, the equivalent inductance $L_{eq} = L_S\text{-}2M^2/L_P$ is defined. As shown in Fig. 8, the following conditions should be satisfied in CC mode:

$$\omega\left(L_S - 2M^2/L_P\right) = \frac{1}{\omega C_{S1}} = \omega L_1 = \omega L_{eq} \tag{4}$$

where ω is the resonant angular frequency of the system, $\omega = 2\pi f$, and the system's frequency is set at $f = 85$ kHz.

As shown in Fig. 8, the load-independent output current can be expressed as

$$\dot{I}_o = \frac{2M\dot{V}_{in}}{j\omega(L_PL_S - 2M^2)}. \tag{5}$$

It can be seen from (5) that L_1 has no relationship to the output current in CC mode. As shown in Fig. 9, the following conditions should be satisfied in CV mode:

$$\begin{cases} \frac{1}{j\omega C'} = \frac{1}{j\omega C_{S2}}//j\omega L_1 \\ \omega\left(L_S - 2M^2/L_P\right) = \frac{1}{\omega C'} = \omega L_{eq} \end{cases} \tag{6}$$

where the symbol "//" represents the parallel connection of impedance.

The load-independent output voltage can be expressed as follows:

$$\dot{V}_o = \frac{2M\dot{V}_{in}}{L_P}. \tag{7}$$

III. Calculation of Equivalent Input Voltage Source and Analysis of Voltage Gain

Due to the unique structure of single-switch *LC*-resonant circuit, the waveform of equivalent input voltage source is different from that of full-bridge circuit. When the MOSFETs or their body diodes are turned ON, the voltage values of C_{P1} and C_{P2} will be clamped in the value of input dc voltage source. When the MOSFETs work at the blocking state, the voltage waveforms of C_{P1} and C_{P2} are determined by the resonant network.

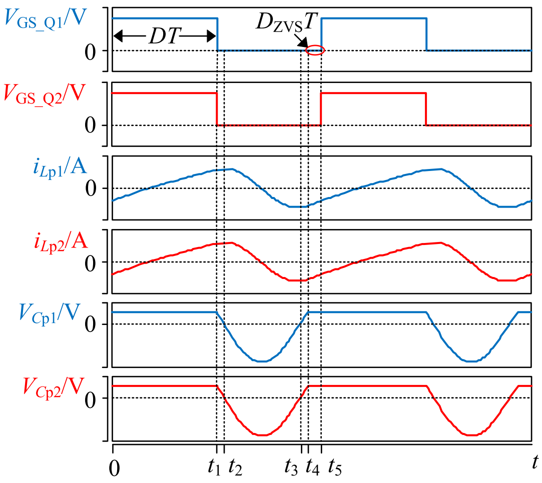

Fig. 10. Relevant voltage and current operating waveforms.

A. Calculation of Equivalent Input AC Voltage Source

The relevant voltage and current waveforms are shown in Fig. 10, V_{GS_Q1} and V_{GS_Q2} are the driving signals of the switches Q_1 and Q_2, respectively. i_{Lp1} and i_{Lp2} are the currents of the transmitting coils. V_{Cp1} and V_{Cp2} are the voltage values of C_{P1} and C_{P2}.

Since the equivalent ac voltage source input to the resonant networks is determined by the voltage waveforms of C_{P1} and C_{P2}, it is necessary to calculate the value of equivalent input ac voltage source.

The voltage waveform of C_{P1} or C_{P2} is shown in Fig. 11. As shown in Fig. 11(a), 0-t_5 is one operating period, V_{dc} is the input dc voltage, and v_{Cpmax} is the peak resonant voltage

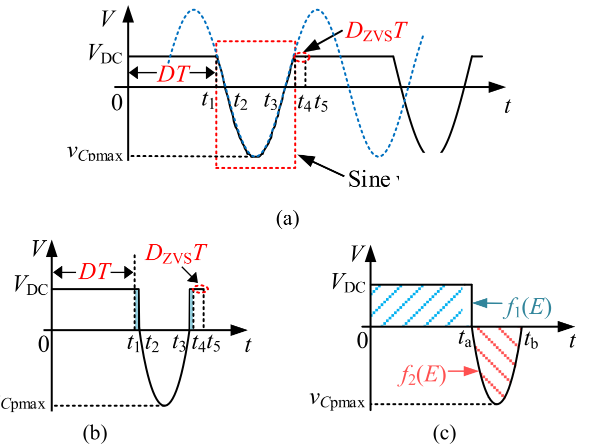

Fig. 11. Voltage waveform of C_{P1} or C_{P2}. (a) Continuous voltage waveform. (b) Equivalent voltage waveform in one operating period. (c) Simplified voltage waveform in one operating period.

of C_{P1} or C_{P2}. To reduce the switching loss, it is necessary to ensure that Q_1 and Q_2 can realize ZVS. ZVS margin is designed, D_{ZVS} represents the ZVS margin, and D is the duty cycle. There are three stages in one operating period, the Q_1 and Q_2 are in forward-conducting state during 0 to t_1, and the voltage values of C_{P1} and C_{P2} are V_{dc}. The Q_1 and Q_2 are in blocking state during the t_1 to t_4, both C_{P1} and C_{P2} are in the resonant state, and the voltage waveform is similar to a sine wave. The Q_1 and Q_2 are in reverse-conducting state during the t_4 to t_5, and the voltage values of C_{P1} and C_{P2} are V_{dc}.

In fact, the proportion of t_1–t_2 and t_3–t_4 in one operating period is small. For the convenience of mathematical analysis, the voltage values of these two periods can be approximately equal to V_{dc}. As shown in Fig. 11(b), it is the equivalent voltage waveform in one operating period. The voltage waveform of t_3–t_5 in Fig. 11(b) is shifted to the left before t_2. Finally, the voltage waveform of C_{P1} or C_{P2} in one operating period can be simplified as shown in Fig. 11(c). For the convenience of analysis, $v_{C\mathrm{pmax}} = E$ is defined. $u_{C\mathrm{p}}(t)$ in one operating period can be expressed as follows:

$$u_{C\mathrm{p}}(t) = \begin{cases} V_{\mathrm{DC}} & (0 < t \le t_{\mathrm{a}}) \\ -E\sin(\omega_1 t + \varphi) & (t_{\mathrm{a}} < t \le t_{\mathrm{b}}). \end{cases} \tag{8}$$

φ can be expressed as follows:

$$\varphi = \frac{-t_{\mathrm{a}}\omega_1}{\pi} \cdot 180^\circ. \tag{9}$$

Assuming $\Delta t = t_4\text{-}t_3 = t_2\text{-}t_1$, Δt can be expressed as follows:

$$\Delta t(E) = \frac{\pi \cdot \arcsin\left(\frac{V_{\mathrm{DC}}}{E}\right)}{180^\circ \cdot \omega_1}. \tag{10}$$

The angular frequency ω_1 can be expressed as follows:

$$\omega_1(E) = \frac{\pi}{t_3 - t_2} = \frac{\pi}{(1 - D - D_{\mathrm{ZVS}})T - 2\Delta t(E)}. \tag{11}$$

As C_{P1} and L_{P1} are in parallel, the average voltage of inductor is zero in one operating period, which is called volt–second balance. As shown in Fig. 11(c), the functional equations of E can be written as

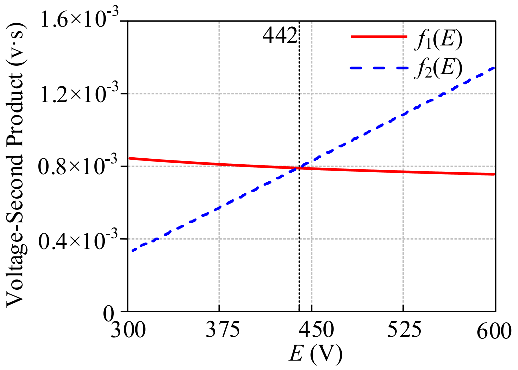

Fig. 12. Diagram of $f_1(E)$ and $f_2(E)$.

$$\begin{cases} f_1(E) = V_{\mathrm{dc}} \cdot [(D + D_{\mathrm{ZVS}})T + 2\Delta t(E)] \\ f_2(E) = \frac{E}{\sqrt{2}} \cdot [(1 - D - D_{\mathrm{ZVS}})T - 2\Delta t(E)]. \end{cases} \tag{12}$$

According to (12), the value of E can be calculated as

$$E = \frac{\sqrt{2}V_{\mathrm{dc}}\,[(D + D_{\mathrm{ZVS}})T + 2\Delta t(E)]}{(1 - D - D_{\mathrm{ZVS}})T - 2\Delta t(E)}. \tag{13}$$

In order to obtain the fundamental component of equivalent input ac voltage source, the voltage waveform in Fig. 11(c) can be decomposed by Fourier series

$$\begin{cases} a_1 = \frac{2}{T}\int_0^{t_a} V_{\mathrm{dc}}\sin(\omega t)dt + \frac{2}{T}\int_{t_a}^{t_b}(-E) \\ \quad \sin(\omega_1 t + \varphi)\sin(\omega t)dt \\ b_1 = \frac{2}{T}\int_0^{t_a} V_{\mathrm{dc}}\cos(\omega t)dt + \frac{2}{T}\int_{t_a}^{t_b}(-E) \\ \quad \sin(\omega_1 t + \varphi)\cos(\omega t)dt \\ c_{\mathrm{o}} = \frac{1}{T}\int_0^{t_a} V_{\mathrm{dc}}dt + \frac{1}{T}\int_{t_a}^{t_b}(-E)\sin(\omega_1 t + \varphi)dt \end{cases} \tag{14}$$

where c_{o} is the dc voltage component contained in the waveform. Through Fourier decomposition of $u_{C\mathrm{p}}(t)$, the fundamental component of $u_{C\mathrm{p}}(t)$ is defined as E_1.

$$E_1 = \sqrt{a_1^2 + b_1^2}. \tag{15}$$

In this article, the partial voltage waveforms of C_{P1} and C_{P2} are treated as sinusoidal waveforms. To ensure the realization of ZVS, $D_{\mathrm{ZVS}} = 9\%$ is designed in this article, the duty cycle $D = 0.5$ remains unchanged, the input dc voltage is 155 V. The intersection point of function $f_1(E)$ and function $f_2(E)$ can be obtained by the Mathcad software, which is the peak resonant voltage of C_{P1} or C_{P2}. The diagram of $f_1(E)$ and $f_2(E)$ is shown in Fig. 12, and the intersection point is 442V, which means $E =$ 442 V.

Theoretically, the maximum voltage stress on Q_1 or Q_2 should be the sum of the input dc voltage and E. Therefore, when the input voltage V_{dc} is 155 V, to achieve 9% ZVS margin, the maximum voltage stress on Q_1 or Q_2 should be about 597 V. Formula (15) is calculated by the Mathcad software, and the fundamental component E_1 of equivalent input ac voltage source is about 253.2 V. The above analysis provides a basis for the specific values of C_{P1} and C_{P2}.

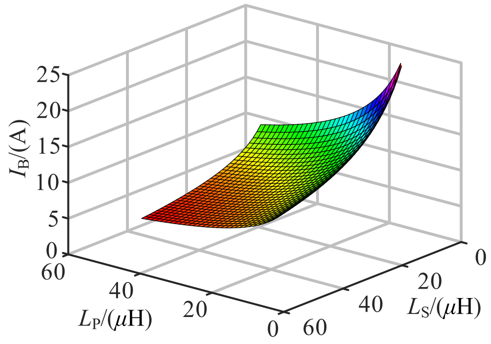

Fig. 13. I_B changing with L_P and L_S in CC mode.

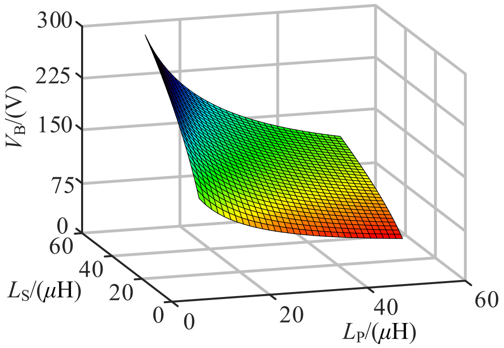

Fig. 14. V_B changing with L_P and L_S in CV mode.

B. Analysis of Voltage Gain and Current Gain

After the parameters of compensation network are determined, according to (5) and (7), when the coupling coefficient $k = 0.31$, the 3-D diagrams of the output current in CC mode and the output voltage in CV mode changing with L_P and L_S can be obtained. From Figs. 13 and 14, the value ranges of L_P and L_S can be obtained for the required output parameters.

Besides, when the parameters of compensation network are determined, the expressions of voltage gain and current gain can be obtained. According to Fig. 8(b), the total impedance Z_1 and the total current $\dot{I}_1$ can be expressed as follows:

$$\begin{cases} Z_1 = j\omega L_{eq} + \frac{R_{eq}+j\omega L_1}{j\omega C_{S1}(R_{eq}+j\omega L_1)+1} \\ \dot{I}_1 = \frac{2M\dot{V}_{in}}{L_P Z_1}. \end{cases} \tag{16}$$

The output ac equivalent resistance R_{eq} can be expressed as follows:

$$\begin{cases} R_{eq} = \frac{8}{\pi^2} R_B \\ R_B = \frac{V_B}{I_B} \end{cases} \tag{17}$$

where R_B is the load resistance; the output current of the compensation network can be calculated as

$$\dot{I}_o = \frac{\dot{I}_1}{1 + j\omega C_{S1}\left(R_{eq} + j\omega L_1\right)}. \tag{18}$$

The output current I_B and current gain G_{CC} in CC mode can be expressed as follows:

$$\begin{cases} I_B = \frac{2i_o}{\pi} \\ G_{CC} = \frac{I_B}{V_{dc}} \end{cases} \tag{19}$$

where i_o is the peak value of ac current before the full-bridge diode rectifier. The output power P_{o1} in CC mode can be expressed as

$$P_{o1} = {I_B}^2 R_B. \tag{20}$$

Similarly, according to Fig. 9(b), the total impedance Z_2 and the output voltage of the compensation network can be calculated as

$$\begin{cases} Z_2 = j\omega L_{eq} + \frac{1}{j\omega C'} + R_{eq} \\ \dot{V}_o = \frac{2M\dot{V}_{in} R_{eq}}{L_P Z_2}. \end{cases} \tag{21}$$

The output voltage V_B and voltage gain G_{CV} in CV mode can be expressed as follows:

$$\begin{cases} V_B = \frac{\pi v_o}{4} \\ G_{CV} = \frac{V_B}{V_{dc}} \end{cases} \tag{22}$$

where v_o is the peak value of ac voltage before the full-bridge diode rectifier. The output power P_{o2} in CV mode can be expressed as

$$P_{o2} = \frac{{V_B}^2}{R_B}. \tag{23}$$

In the WPT system, the power losses are mainly concentrated in the transmitting and receiving coils, inductor, MOSFETs, and rectifier diodes; the efficiency η of the system is expressed as

$$\begin{cases} \eta = \frac{P_o}{P_{coil}+{I_{L1}}^2 r_{L1}+r_{ds}({I_{Q1}}^2+{I_{Q2}}^2)+2V_d I_d+P_o} \\ P_{coil} = {I_{P1}}^2 r_{p1} + {I_{P2}}^2 r_{p2} + {I_S}^2 r_s \end{cases} \tag{24}$$

where P_o represents the output power in CC or CV mode, and P_{coil} is the total loss of the coils. I_{P1}, I_{P2}, I_S, and I_{L1} are the currents of two transmitting coils, the receiving coil, and inductor L_1, respectively. r_{p1}, r_{p2}, r_s, r_{ds}, and r_{L1} are the parasitic resistances of the transmitters, the receiver, MOSFETs, and inductor L_1, respectively. I_{Q1}, I_{Q2}, and I_d are the currents of Q_1, Q_2, and the rectifier diodes, and V_d is the forward voltage drop of the rectifier diode

$$\begin{cases} \dot{I}_{P1} = \frac{\dot{V}_{in}}{r_{p1}+j\omega L_{P1}+\frac{\omega^2 {M_{1S}}^2}{Z_S}} \\ \dot{I}_{P2} = \frac{\dot{V}_{in}}{r_{p2}+j\omega L_{P2}+\frac{\omega^2 {M_{2S}}^2}{Z_S}} \\ \dot{I}_{S1} = \frac{2M\dot{V}_{in}}{L_P Z_1} \\ \dot{I}_{S2} = \frac{2M\dot{V}_{in}}{L_P Z_2} \end{cases} \tag{25}$$

where Z_S is the total impedance of the secondary-side, and I_{S1} and I_{S2} are the currents of the receiving coil in CC mode and CV mode, respectively.

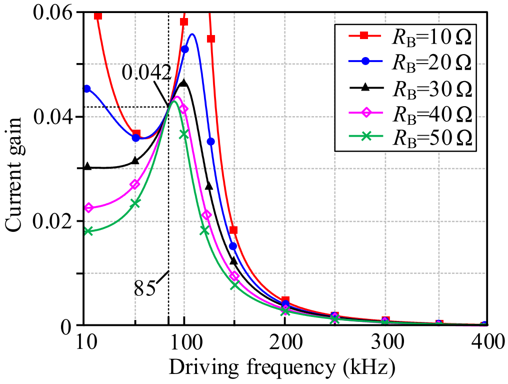

Fig. 15. Curve of G_{CC} versus driving frequency in CC mode.

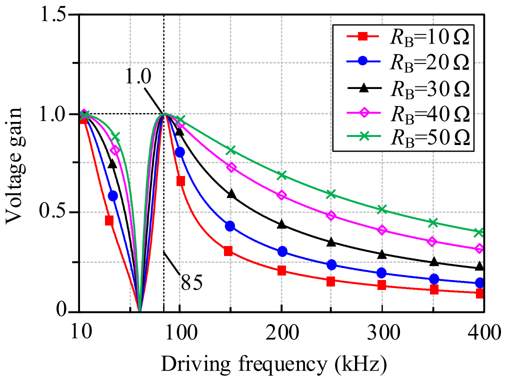

Fig. 16. Curve of G_{CV} versus driving frequency in CV mode.

The total impedances of secondary side are defined as Z_{S1} and Z_{S2} in CC mode and CV mode, separately.

$$\begin{cases} Z_{S1} = j\omega L_S + \frac{R_{eq}+j\omega L_1}{j\omega C_{S1}(R_{eq}+j\omega L_1)+1} \\ Z_{S2} = j\omega L_S + \frac{j\omega L_1}{1-\omega^2 L_1 C_{S2}} + R_{eq}. \end{cases} \tag{26}$$

The currents of the rectifier diodes, the inductor L_1, and MOSFETs can be expressed as

$$\begin{cases} I_{Q1} = \sqrt{\frac{1}{T}\int_0^{DT} i_{Q1}(t)\mathrm{d}t} \approx I_{Q2} \\ \dot{I}_{d1} = \dot{I}_{L11} = \frac{2M\dot{V}_{in}}{j\omega(L_P L_S - 2M^2)} \\ \dot{I}_{d2} = \dot{I}_{S2} \\ \dot{I}_{L12} = \frac{\dot{I}_{S2}}{1-\omega^2 L_1 C_{S2}} \end{cases} \tag{27}$$

where I_{d1} and I_{d2} are the currents of the rectifier diodes in CC mode and CV mode, I_{L11} and I_{L12} are the currents of inductor L_1 in CC mode and CV mode, and $i_{Q1}(t)$ is the current on switch Q_1.

According to (19) and (22), the curves of G_{CC} and G_{CV} versus driving frequency can be drawn. As shown in Fig. 15, it can be seen that the current gain G_{CC} remains unchanged at k = 85 kHz when R_B changes from 10 to 50 Ω, the G_{CC} is 0.042 at k = 85 kHz, which means when the input dc voltage is 155 V, the output current will be 6.5 A. The current gain is smaller in higher harmonics. As shown in Fig. 16, it can be seen that the voltage gain G_{CV} remains unchanged at k = 85 kHz when R_B changes from 10 to 50 Ω and G_{CV} is 1 at k = 85 kHz, which means when the input voltage is 155 V, the output voltage will be 155 V.

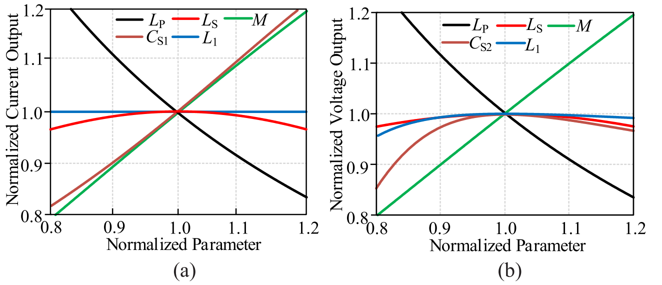

Fig. 17. Normalized output with varying normalized parameters. (a) Curves in CC mode when R_B is set as 24 Ω. (b) Curves in CV mode when R_B is set as 24 Ω.

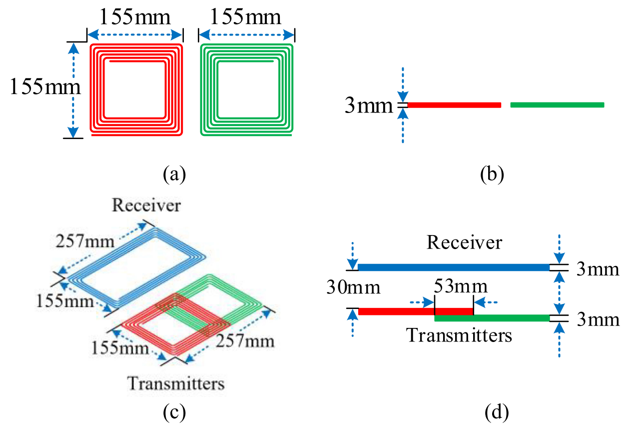

Fig. 18. Sizes of the transmitters and the receiver.

The BP pad is composed of two identical and partially overlapped coils. In order to test the influence of compensation parameters on the output, the sensitivity analysis of the system is carried out. As shown in Fig. 17, it is the normalized output with varying normalized parameters when R_B is set as 24 Ω. As shown in Fig. 17(a), it can be seen that the variation of L_1 has no relationship to the current gain in CC mode. As shown in Fig. 17(b), it can be seen that the variations of L_1 and L_S are not sensitive to the output voltage in CV mode. From Fig. 17, the circuit parameters can be better designed.

IV. PARAMETER DESIGN OF THE PROPOSED CIRCUIT

In this article, the BP pad is selected as the transmitters; the sizes of the transmitters and the receiver are shown in Fig. 18.

From Fig. 18, the BP pad consists of two identical square coils, the side length of each square coil is 155 mm, all coils are made of Litz wires, and the outer diameter of the wire is 3 mm. In practice, the overlap between the two transmitting coils is adjusted to ensure zero mutual coupling between them. As shown in Fig. 18(c) and (d), when the overlap reaches 53 mm, decoupling of overlapped coils can be achieved.

The model of the magnetic coupler is shown in Fig. 19, and the designed dimensional parameters of magnetic coupler are shown in Table I.

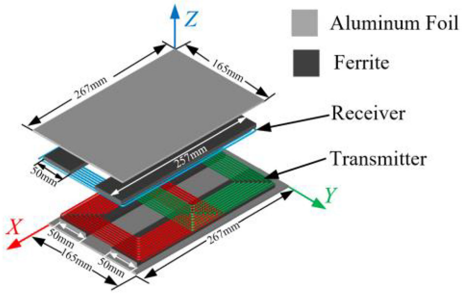

Fig. 19. Model of the magnetic coupler.

TABLE I
DESIGNED DIMENSIONAL PARAMETERS OF MAGNETIC COUPLER

Parameters	Values
Turns per coil	N_{P1}:10, N_{P2}:10, N_S:8
Air gap distance	30mm
L_{P1} coil dismensions	155mm×155mm×3mm
L_{P2} coil dismensions	155mm×155mm×3mm
L_S coil dismensions	257mm×155mm×3mm
Primary ferrite dismensions	257mm×50mm×1mm
Primary shield dismensions	267mm×160mm×0.2mm
Secondary ferrite dismensions	257mm×50mm×1mm
Secondary shield dismensions	267mm×160mm×0.2mm

TABLE II
ESSENTIAL PARAMETERS OF THE WPT SYSTEM

Symbol	Definition	Value
U_{DC}	Input DC voltage	155V
f	Operating frequency	85kHz
I_B	Output current in constant-current mode	6.5A
V_B	Output voltage in constant-voltage mode	155V
P_B	Output power	250W-1kW

The essential parameters of the WPT system are shown in Table II. The voltage waveform of C_{P1} and ZVS conditions are analyzed in Section III-A. When the input dc voltage is 155 V, if 9% ZVS margin is realized, the maximum voltage stress on Q_1 or Q_2 should be about 597 V. The theoretical analysis provides a basis for the values of C_{P1} and C_{P2}. As shown in Fig. 21, the SABER software can be used to scan the V_{DS_Q1} waveforms under different C_{P1} values. With the increase of C_{P1} values, V_{DS_Q1max} is decreasing, and the ZVS margin becomes smaller until the ZVS margin disappears. From Fig. 20, when $C_{P1} = 57.5$ nF, V_{DS_Q1max} is close to 597 V in CC mode, and the ZVS margin is approximately 8.1%, which is close to the designed value in Section III-A.

Fourier decomposition diagram of the voltage V_{Cp1} is shown in Fig. 21; the values of the calculation and the simulation results match well and thus validate the correctness of the theoretical analysis in Section III-A.

In addition, the influence of C_{P1} values on the V_{DS_Q1} waveforms can be analyzed qualitatively; the simplified circuit model is shown in Fig. 22.

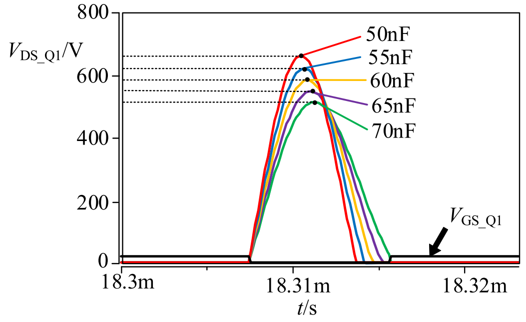

Fig. 20. Waveforms of V_{DS_Q1} versus C_{P1} values when $R_B = 24\ \Omega$ in simulation.

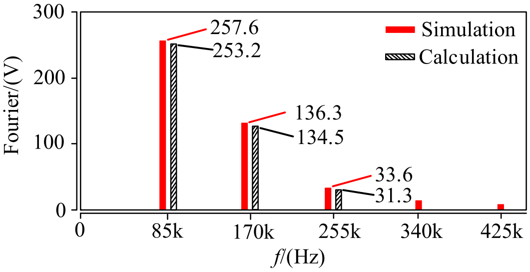

Fig. 21. Fourier decomposition diagram of the voltage V_{Cp1} in CC mode.

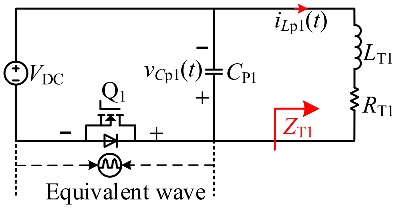

Fig. 22. Simplified circuit model.

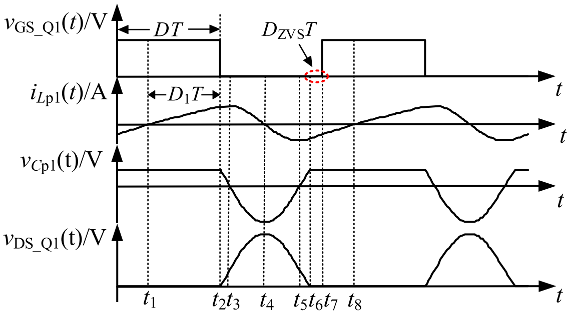

Fig. 23. Waveforms of the operation states.

The total input impedance Z_{T1} in CC mode can be expressed as

$$\begin{cases} Z_X = (R_{eq} + j\omega L_1)//\frac{1}{j\omega C_{S1}} + j\omega(L_S - M_{1S}) \\ Z_{T1} = Z_X//j\omega M_{1S} + j\omega(L_{P1} - M_{1S}) = R_{T1} + j\omega L_{T1}. \end{cases} \tag{28}$$

The waveforms of the operation states are shown in Fig. 23. It can be seen that $i_{Lp}(t_1) = 0$, the charging time of L_{T1} equals to $D_1 T$, and it should be noted that $D_1 \leq D$. $i_{Lp}(t_1)$ can be expressed as follows:

$$i_{Lp1}(t) = \frac{V_{\rm dc}}{R_{\rm T1}}\left(1 - e^{\frac{R_{\rm T1}}{L_{\rm T1}}t}\right)(t_1 < t < t_2). \tag{29}$$

When the driving signal of Q$_1$ turns OFF at t_2, the $C_{\rm P1}$, $L_{\rm T1}$, and $R_{\rm T1}$ will have zero input response; the state equation of $v_{\rm DS\_Q1}(t)$ and $i_{Lp1}(t)$ can be expressed as

$$\begin{cases} -C_{\rm P1}\frac{dv_{C\rm p1}(t)}{dt} = i_{L\rm p1}(t) \\ v_{C\rm p1}(t) = H(D_1)\cdot e^{-\alpha t}\cos\left[\omega_{\rm d}t + \varphi(D_1)\right](t_2 \le t \le t_6) \\ v_{\rm DS\_Q1}(t) = -v_{C\rm p1}(t) + V_{\rm dc} \end{cases} \tag{30}$$

where the coefficients α, $\omega_{\rm d}$, H, and φ can be written as

$$\begin{cases} \alpha = \frac{R_{\rm T1}}{2L_{\rm T1}} \\ \omega_{\rm d} = \sqrt{\frac{1}{L_{\rm T1}C_{\rm P1}} - \frac{{R_{\rm T1}}^2}{4{L_{\rm T1}}^2}} \\ H(D_1) = \sqrt{{V_{\rm dc}}^2 + \frac{\left(\frac{i_{Lp1}(D_1T)}{C_{\rm P1}} + V_{\rm dc}\alpha\right)^2}{{\omega_{\rm d}}^2}} \\ \varphi(D_1) = -\arctan\frac{H(D_1)}{V_{\rm dc}}. \end{cases} \tag{31}$$

From Fig. 23, the switch Q$_1$ is in reverse conducting state during the t_6–t_7. At time t_7, the drive signal of Q$_1$ arrives, and the switch Q$_1$ realizes ZVS.

$$\begin{cases} i_{Lp1}(t_7) \le 0 \\ v_{Cp1}(t_7) = V_{\rm dc}. \end{cases} \tag{32}$$

There are three stages in one operating period: the conduction time of Q$_1$ (0-t_2), the time of zero input response (t_2–t_6), and the time of ZVS margin (t_6–t_7). When the switching frequency of Q$_1$ is 85 kHz, the duty cycle D is 0.5, the $D_{\rm ZVS}$ is 0.09, the time of zero input response is $(t_6 - t_2) = (1 - D - D_{\rm ZVS})\ T = 4.82 \times 10^{-6}$ s. As the value of E has been calculated as 442 V by (13) in Section III-A, the maximum voltage stress on Q$_1$ should be about 597 V.

To get the exact value of $C_{\rm P1}$, the values of $i_{Lp1}(D_1t)$ and $C_{\rm P1}$ can be iterated in the Mathcad software until the two conditions are met.

1) The value of $i_{LP1}(D_1T)$ in (31) can be changed to make the peak value of $v_{\rm DS\_Q1}(t)$ equal to 597 V.
2) The value of $C_{\rm P1}$ can be changed to make $v_{\rm DS\_Q1}$ (4.82×10^{-6}) equal to zero.

According to (30), the waveform of $v_{\rm DS\_Q1}(t)$ can be drawn as Fig. 24; the $C_{\rm P1}$ can be calculated as 56 nF; and the qualitative analysis and the simulation results match well.

Based on above analysis, the parameters of the compensation network are designed; the actual values of the measured parameters of the compensation network are shown in Table III.

V. EXPERIMENTAL VERIFICATION

In order to verify the previous analysis and designs, a 1-kW experimental WPT prototype was configured. The major components of the prototype are shown in Fig. 25.

From Fig. 25, the prototype consists of the primary circuit, loosely coupled transformer, the secondary circuit, electronic load, oscilloscopes and digital multimeters. Q$_1$ and Q$_2$ are SiC MOSFETs (CGE1M120080), and the secondary rectifier diodes are DPG30C300HB. The system is powered by a dc voltage

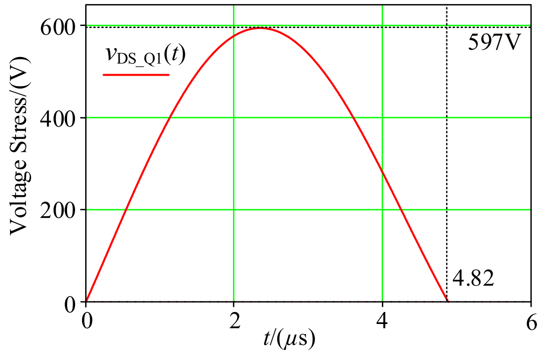

Fig. 24. Waveform of $v_{\rm DS\_Q1}(t)$ obtained by qualitative analysis.

TABLE III
PARAMETERS OF COMPENSATION NETWORK

Symbol	Definition	Value
$C_{\rm P1}$	Resonant capacitance at the primary-side	57.54 nF
$C_{\rm P2}$	Resonant capacitance at the primary-side	57.51 nF
$L_{\rm P1}$	Inductance of the transmitter coil	30.12 μH
$L_{\rm P2}$	Inductance of the transmitter coil	30.08 μH
$L_{\rm S}$	Inductance of the receiving coil	41.2 μH
$r_{\rm p1}$	Parasitic resistance of $L_{\rm P1}$	89 mΩ
$r_{\rm p2}$	Parasitic resistance of $L_{\rm P2}$	87 mΩ
$r_{\rm s}$	Parasitic resistance of $L_{\rm S}$	108 mΩ
$C_{\rm S1}$	Resonant capacitance at the secondary-side	105.8 nF
$C_{\rm S2}$	Resonant capacitance at the secondary-side	211.6 nF
L_1	Resonant inductance at the secondary-side	33.38 μH
r_{L1}	Parasitic resistance of L_1	132 mΩ
$M_{\rm 1S}$	Mutual inductance between $L_{\rm P1}$ and $L_{\rm S}$	10.87 μH
$M_{\rm 2S}$	Mutual inductance between $L_{\rm P2}$ and $L_{\rm S}$	10.85 μH
$D_{\rm ZVS}$	ZVS margin	0.09
D	Duty cycle	0.5

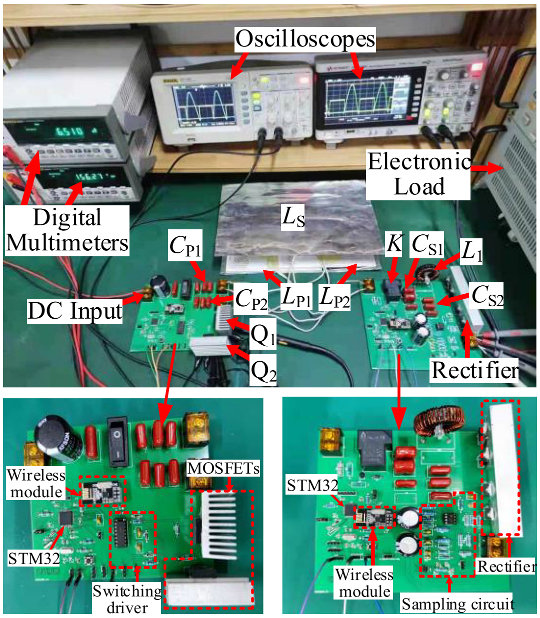

Fig. 25. Exterior appearance of the proposed WPT prototype.

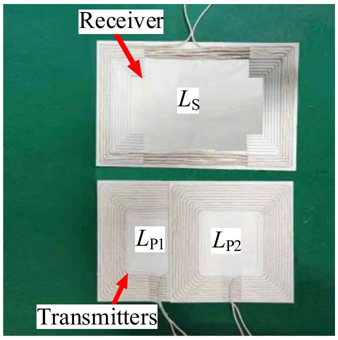

Fig. 26. Transmitters and the receiver wound with Litz wires.

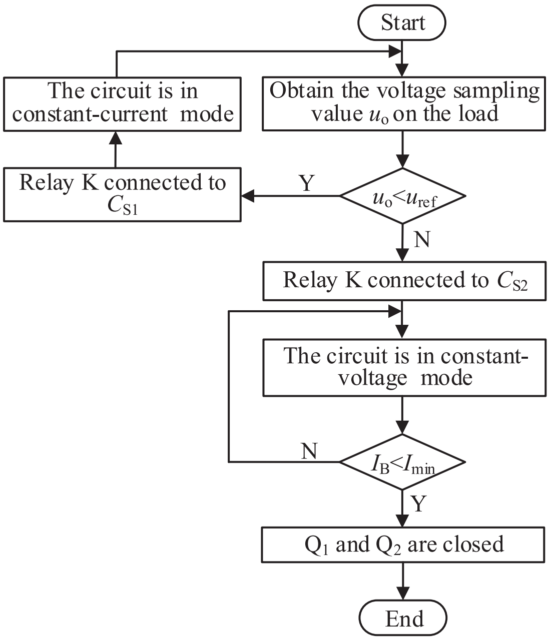

Fig. 27. Control flowchart of the proposed WPT system for CC and CV modes.

source. Metallized polypropylene film capacitors (CBB) are used as compensation components. The STM32F103 is used to generate switching signals for the inverters and the relay K. As shown in Fig. 26, the transmitters and the receiver were wound with Litz wires. The mutual inductances, self-inductances, and parasitic resistances of the transmitters and receiver were measured by Agilent 4263B *LC*R meter. The SPDT relay (953-1C-12DG-1) in the secondary circuit is used to switch the compensation networks to achieve CC output and CV output. The control signals (start/stop) are transmitted from the secondary circuit to the primary circuit via the wireless module (NRF24L01). Due to the limitation of experimental conditions, the battery is replaced by the electronic load as the load.

The control flowchart of the proposed WPT system for CC and CV modes is shown in Fig. 27, u_{ref} is the critical reference voltage at the conversion point between CC and CV modes, $I_{\min}$ is the lower limit of the output current. After the WPT system is initialized and started, the output voltage V_B and current I_B are acquired via the sampling circuits; when the sampling voltage u_o is lower than the reference value u_{ref}, the switching signals are generated to drive the two MOSFETs (Q_1, Q_2), the system is in the CC mode, and the signal is not sent to drive the relay K. When the sampling value u_o is higher than or equal to the reference value u_{ref}, the signal is sent to drive the relay K, and the CV mode is selected. With the load R_B increasing in CV mode, the output current decreases gradually. When the output current I_B is lower than the $I_{\min}$, the control signal is transmitted from the secondary circuit to the primary circuit via the wireless module, and the driving signals of Q_1 and Q_2 will turn OFF.

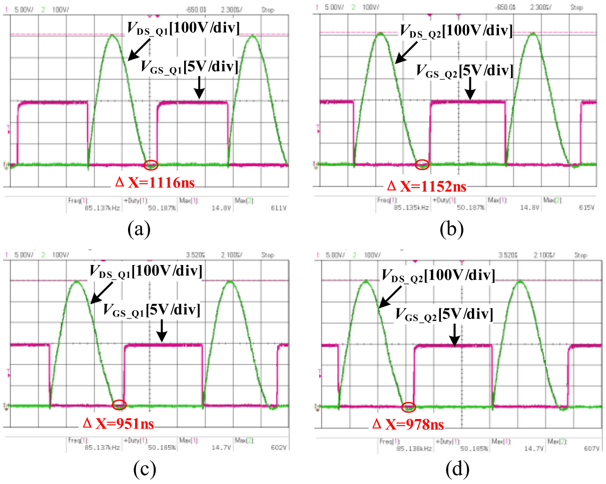

(a) (b)

(c) (d)

Fig. 28. ZVS waveforms in CC mode. (a) ZVS waveform of Q_1 when $R_B = 6\ \Omega$. (b) ZVS waveform of Q_2 when $R_B = 6\ \Omega$. (c) ZVS waveform of Q_1 when $R_B = 24\ \Omega$. (d) ZVS waveform of Q_2 when $R_B = 24\ \Omega$.

In the experiments, the output power range is 250—1000 W, the variation of the load resistance is 6—24 Ω in CC mode, and the variation of the load resistance is 24—96 Ω in CV mode. In order to verify that ZVS can be realized in the experiments, the ZVS waveforms were measured under the minimum and the maximum load conditions in CC and CV modes.

The ZVS waveforms in CC mode are shown in Fig. 28. The ZVS waveforms of Q_1 and Q_2 are shown in Fig. 28(a) and (b); when $R_B = 6\ \Omega$, the ZVS margins ($\Delta X \cdot f$) of Q_1 and Q_2 can be computed as 9.48% and 9.79%, respectively. The ZVS waveforms of Q_1 and Q_2 are shown in Fig. 28(c) and (d); when $R_B = 24\ \Omega$, the ZVS margins of Q_1 and Q_2 can be computed as 8.08% and 8.31%.

The ZVS waveforms in CV mode are shown in Fig. 29. The ZVS waveforms of Q_1 and Q_2 are shown in Fig. 29(a) and (b); when $R_B = 24\ \Omega$, the ZVS margins of Q_1 and Q_2 can be computed as 9.28% and 8.98%, respectively. The variation of D_{ZVS} after switching from CC mode to CV mode is little. The ZVS waveforms of Q_1 and Q_2 are shown in Fig. 29(c) and (d); when $R_B = 9\ 6\Omega$, the ZVS margins of Q_1 and Q_2 can be computed as 7.13% and 6.97%. The design of ZVS margin ensures the ZVS of switches Q_1 and Q_2.

As shown in Fig. 30, the performance of the proposed WPT system is tested when the load is suddenly changed. It can be found in Fig. 30(a) and (b) that the proposed WPT system can maintain a constant output current in the CC mode and a constant output voltage in the CV mode.

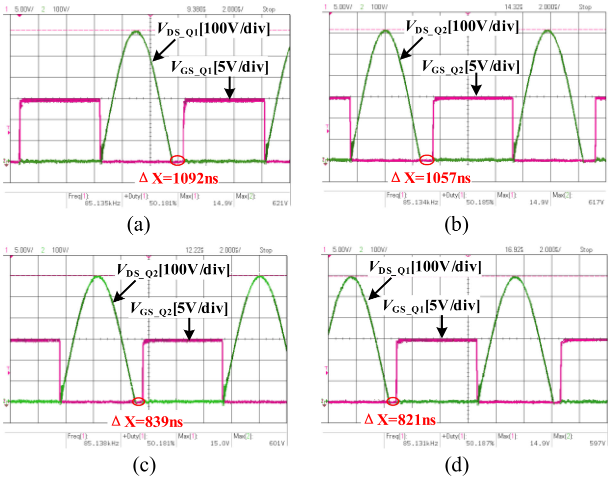

(a) (b)

(c) (d)

Fig. 29. ZVS waveforms in CV mode. (a) ZVS waveform of Q_1 when $R_B = 24\ \Omega$. (b) ZVS waveform of Q_2 when $R_B = 24\ \Omega$. (c) ZVS waveform of Q_1 when $R_B = 96\ \Omega$. (d) ZVS waveform of Q_2 when $R_B = 96\ \Omega$.

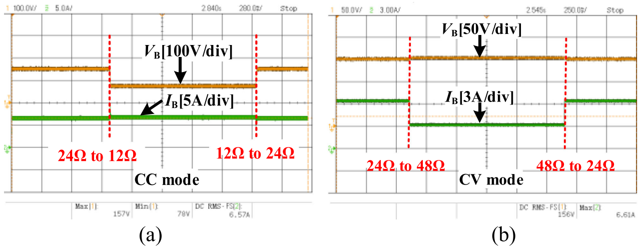

(a) (b)

Fig. 30. Dynamic performance of the proposed WPT system. (a) In CC mode when the load changes from 12 to 24 Ω. (b) In CV mode when load changes from 24 to 48 Ω.

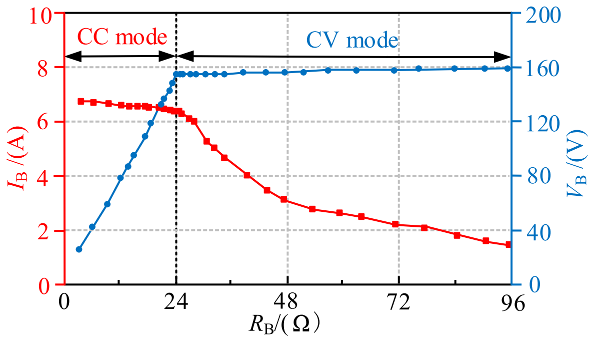

Fig. 31. Measured output characteristics versus the load.

Fig. 31 gives the measured output currents and voltages versus the load. As shown in Fig. 32, the input parameters are obtained by the ac/dc digital power meter (PZ9902U), and the output parameters are obtained by the electronic load (IT8616); the maximum efficiency is 92.5% when $R_B = 24\ \Omega$ in CC mode. The diagram of efficiency η versus the load is shown in Fig. 33. As the current flowing through the coils increases when switching from CC mode to CV mode, the loss increases, so the efficiency sag at the mode transition. The maximum efficiency is 91.3% in CV mode.

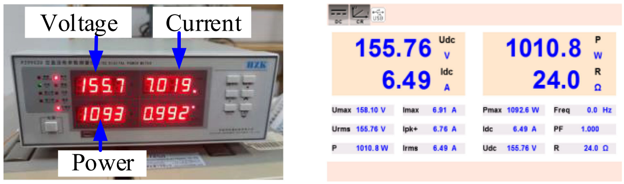

(a) (b)

Fig. 32. Measured input and output parameters when $R_B = 24\ \Omega$ in CC mode. (a) Input parameters. (b) Output parameters.

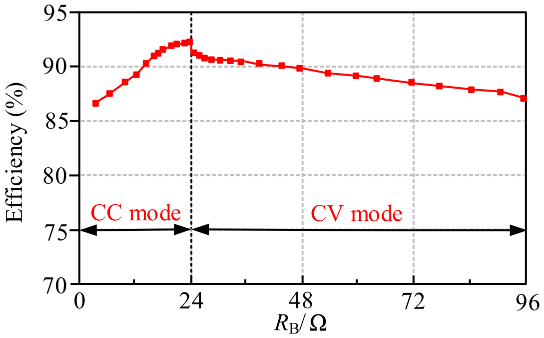

Fig. 33. Diagram of efficiency versus the load.

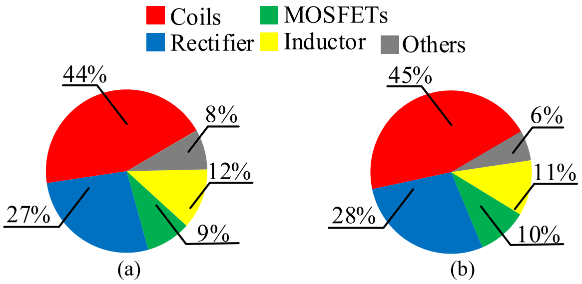

(a) (b)

Fig. 34. Power loss distribution with $R_B = 24\ \Omega$. (a) Power loss distribution in CC mode. (b) Power loss distribution in CV mode.

TABLE IV
PERFORMANCE COMPARISON OF SINGLE-SWITCH CIRCUIT

Reference	Input DC Voltage	Output Power	CC/CV	Efficiency
Proposed	155V	1000W	CC and CV	92.5%
[14]	150V	60W	CC and CV	78.2%
[15]	100V	450W	CC and CV	90.3%
[16]	5V	11W	CV	86.4%
[17]	48V	350W	CV	87.1%
[18]	48V	214W	CV	86.7%
[19]	35V	27.8W	CC	74.8%

The detailed analysis of circuit power loss in both CC and CV modes is shown in Fig. 34. It can be seen that the loss distribution changes little in the two modes, and the main loss distribution of the system is the coils and rectifier diodes.

As shown in Table IV, the performance of the work in this article is compared with other existing single-switch circuit-based WPT. It can be seen that the proposed input-parallel topology based on single-switch *LC*-resonant circuit can achieve higher efficiency.

IV. CONCLUSION

In this article, a novel topology of input-parallel structure based on single-switch *LC*-resonant circuit with CC output and CV output is proposed. The parallel structure avoids input voltage unbalance and simplifies the equivalent circuit model. It has been verified the output power of the traditional single-switch *LC*-resonant circuit can be further increased through the parallel structure. Besides, the proposed topology prevents shoot-through of power switches, which improves the stability of the WPT system. By decoupling the transmitters, each inverter drives an independent primary coil to transfer energy to the common secondary coil; the analysis and calculation are simplified. CC and CV output modes can be achieved by controlling one SPDT relay without adding dc–dc converters or changing the switching frequency of MOSFETs. Finally, a 1-kW experimental WPT prototype was configured; ZVS can be realized when the load changes from 6 to 96 Ω in the experiments; and the feasibility of the theoretical analysis is verified by the simulations and experiments; the maximum efficiency is 92.5%.

REFERENCES

[1] X. Dai, J. Wu, J. Jiang, R. Gao, and U. K. Madawala, “An energy injection method to improve power transfer capability of bidirectional WPT system with multiple pickups,” *IEEE Trans. Power Electron.*, vol. 36, no. 5, pp. 5095–5107, May 2021.

[2] Y. Sun, H. Zhang, A. P. Hu, C. Tang, and L. Xiang, “The recognition and control of nonideal soft-switching frequency for wireless power transfer system based on waveform identification,” *IEEE Trans. Power Electron.*, vol. 32, no. 8, pp. 6617–6627, Aug. 2017.

[3] K. Song *et al.*, “Design of DD coil with high misalignment tolerance and low EMF emissions for wireless electric vehicle charging systems,” *IEEE Trans. Power Electron.*, vol. 35, no. 9, pp. 9034–9045, Sep. 2020.

[4] V. Z. Barsari, D. J. Thrimawithana, and G. A. Covic, “An inductive coupler array for in-motion wireless charging of electric vehicles,” *IEEE Trans. Power Electron.*, vol. 36, no. 9, pp. 9854–9863, Sep. 2021.

[5] V. X. Thai, G. C. Jang, S. Y. Jeong, J. H. Park, Y.-S. Kim, and C. T. Rim, “Symmetric sensing coil design for the blind-zone free metal object detection of a stationary wireless electric vehicles charger,” *IEEE Trans. Power Electron.*, vol. 35, no. 4, pp. 3466–3477, Apr. 2020.

[6] L. Zhao, D. J. Thrimawithana, U. K. Madawala, A. P. Hu, and C. C. Mi, “A misalignment-tolerant series-hybrid wireless EV charging system with integrated magnetics,” *IEEE Trans. Power Electron.*, vol. 34, no. 2, pp. 1276–1285, Feb. 2019.

[7] B. Song, S. Cui, Y. Li, and C. Zhu, “A fast and general method to calculate mutual inductance for EV dynamic wireless charging system,” *IEEE Trans. Power Electron.*, vol. 36, no. 3, pp. 2696–2709, Mar. 2021.

[8] P. Zhang, M. Saeedifard, O. C. Onar, Q. Yang, and C. Cai, “A field enhancement integration design featuring misalignment tolerance for wireless EV charging using *LCL* topology,” *IEEE Trans. Ind. Electron.*, vol. 36, no. 4, pp. 3852–3867, Apr. 2021.

[9] J. Zhou, B. Zhang, W. Xiao, D. Qiu, and Y. Chen, “Nonlinear parity time-symmetric model for constant efficiency wireless power transfer: Application to a drone-in-flight wireless charging platform,” *IEEE Trans. Ind. Electron.*, vol. 66, no. 5, pp. 4097–4107, May 2019.

[10] J. M. Arteaga, S. Aldhaher, G. Kkelis, C. Kwan, D. C. Yates, and P. D. Mitcheson, “Dynamic capabilities of multi-MHz inductive power transfer systems demonstrated with batteryless drones,” *IEEE Trans. Power Electron.*, vol. 34, no. 6, pp. 5093–5104, Jun. 2019.

[11] C. Liu, C. Jiang, J. Song, and K. T. Chau, “An effective sandwiched wireless power transfer system for charging implantable cardiac pacemaker,” *IEEE Trans. Ind. Electron.*, vol. 66, no. 5, pp. 4108–4117, May 2019.

[12] R. Sedehi *et al.*, “A wireless power method for deeply implanted biomedical devices via capacitively coupled conductive power transfer,” *IEEE Trans. Power Electron.*, vol. 36, no. 2, pp. 1870–1882, Feb. 2021.

[13] N. Hassan, S.-W. Hong, and B. Lee, “A robust multioutput self-regulated rectifier for wirelessly powered biomedical applications,” *IEEE Trans. Ind. Electron.*, vol. 68, no. 6, pp. 5466–5472, Jun. 2021.

[14] Y.-D. Lee, K.-W. Kim, and G.-W. Moon, “A self-compensated planar coil with integrated single-switch regulator for wireless power transfer (WPT) systems,” *IEEE Trans. Power Electron.*, vol. 36, no. 10, pp. 10954–10958, Oct. 2021, doi: 10.1109/TPEL.2021.3066413

[15] H. Li, Y. Yang, J. Chen, J. Xu, M. Liu, and Y. Wang, “A hybrid class e topology with constant current and constant voltage output for light EVs wireless charging application,” *IEEE Trans. Transp. Electrific.*, vol. 7, no. 4, pp. 2168–2180, Dec. 2021, doi: 10.1109/TTE.2021.3083363

[16] Y. Huang, A. T. L. Lee, S.-C. Tan, and S. Y. Hui, “Highly efficient wireless power transfer system with single-switch step-up resonant inverter,” *IEEE J. Emerg. Sel. Topics Power Electron.*, vol. 9, no. 1, pp. 1157–1168, Feb. 2021.

[17] X. Huang, Y. Kong, Z. Ouyang, W. Chen, and S. Lin, “Analysis and comparison of push–pull Class-E inverters with magnetic integration for megahertz wireless power transfer,” *IEEE Trans. Power Electron.*, vol. 35, no. 1, pp. 565–577, Jan. 2020.

[18] X. Huang, Y. Dou, S. Lin, Y. Tian, Z. Ouyang, and M. A. E. Andersen, “Synchronous push–pull Class E rectifiers with load-independent operation for megahertz wireless power transfer,” *IEEE Trans. Power Electron.*, vol. 36, no. 6, pp. 6351–6363, Jun. 2021.

[19] M. Liu, M. Fu, Y. Wang, and C. Ma, “Battery cell equalization via megahertz multiple-receiver wireless power transfer,” *IEEE Trans. Power Electron.*, vol. 33, no. 5, pp. 4135–4144, May 2018.

[20] S. Aldhaher, D. C. Yates, and P. D. Mitcheson, “Load-independent class E/EF inverters and rectifiers for MHz-switching applications,” *IEEE Trans. Power Electron.*, vol. 33, no. 10, pp. 8270–8287, Oct. 2018.

[21] Y. Huang, S. Tan, and S. Y. Hui, “Multiphase-interleaved high step-up dc/dc resonant converter for wide load range,” *IEEE Trans. Power Electron.*, vol. 34, no. 8, pp. 7703–7718, Aug. 2019.

[22] H. Tebianian, Y. Salami, B. Jeyasurya, and J. E. Quaicoe, “A 13.56-MHz full-bridge Class-D ZVS inverter with dynamic dead-time control for wireless power transfer systems,” *IEEE Trans. Ind. Electron.*, vol. 67, no. 2, pp. 1487–1497, Feb. 2020.

[23] H. Li, K. Wang, J. Fang, and Y. Tang, “Pulse density modulated ZVS full-bridge converters for wireless power transfer systems,” *IEEE Trans. Power Electron.*, vol. 34, no. 1, pp. 369–377, Jan. 2019.

[24] S. Samanta, A. K. Rathore, and D. J. Thrimawithana, “Bidirectional current-fed half-bridge (C) (*LC*)–(*LC*) configuration for inductive wireless power transfer system,” *IEEE Trans. Ind. Appl.*, vol. 53, no. 4, pp. 4053–4062, Jul./Aug. 2017.

[25] N. K. Trung, T. Ogata, S. Tanaka, and K. Akatsu, “Attenuate influence of parasitic elements in 13.56-MHz inverter for wireless power transfer systems,” *IEEE Trans. Power Electron.*, vol. 33, no. 4, pp. 3218–3231, Apr. 2018.

[26] Q. Deng, P. Sun, W. Hu, D. Czarkowski, M. K. Kazimierczuk, and H. Zhou, “Modular parallel multi-inverter system for high-power inductive power transfer,” *IEEE Trans. Power Electron.*, vol. 34, no. no.10, pp. 9422–9434, Oct. 2019.

[27] Q. Deng *et al.*, “Multi-inverter phase-shifted control for IPT with overlapped transmitters,” *IEEE Trans. Power Electron.*, vol. 36, no. 8, pp. 8799–8811, Aug. 2021.

[28] Y. Li, R. Mai, L. Lu, and Z. He, “Active and reactive currents decomposition-based control of angle and magnitude of current for a parallel multiinverter IPT system,” *IEEE Trans. Power Electron.*, vol. 32, no. 2, pp. 1602–1614, Feb. 2017.

[29] H. Zhou *et al.*, “Input-series output-equivalent-parallel multi-inverter system for high-voltage and high-power wireless power transfer,” *IEEE Trans. Power Electron.*, vol. 36, no. 1, pp. 228–238, Jan. 2021.

[30] R. Mai, Z. Yan, Y. Chen, S. Liu, and Z. He, "A hybrid transmitter-based efficiency improvement controller with full-bridge dual resonant tank for misalignment condition," *IEEE Trans. Power Electron.*, vol. 35, no. 1, pp. 1124–1135, Jan. 2020.

[31] F. Chen, P. C. Young, H. Garnier, Q. Deng, and M. K. Kazimierczuk, "Data-driven modeling of wireless power transfer systems with multiple transmitters," *IEEE Trans. Power Electron.*, vol. 35, no. 11, pp. 11363–11379, Nov. 2020.

[32] J. Song, M. Liu, and C. Ma, "Analysis and design of a high-efficiency 6.78-MHz wireless power transfer system with scalable number of receivers," *IEEE Trans. Ind. Electron.*, vol. 67, no. 10, pp. 8281–8291, Oct. 2020.

[33] S. Sun, B. Zhang, C. Rong, X. Shu, and Z. Wei, "A multi-receiver wireless power transfer system using self-oscillating source composed of ZVS full-bridge inverter," *IEEE Trans. Ind. Electron.*, to be published, doi: 10.1109/TIE.2021.3066931.

[34] Z. Zhang, X. Li, H. Pang, H. Komurcugil, Z. Liang, and R. Kennel, "Multiple-frequency resonating compensation for multichannel transmission of wireless power transfer," *IEEE Trans. Power Electron.*, vol. 36, no. 5, pp. 5169–5180, May 2021.

[35] S. Huh and D. Ahn, "Two-transmitter wireless power transfer with optimal activation and current selection of transmitters," *IEEE Trans. Power Electron.*, vol. 33, no. 6, pp. 4957–4967, Jun. 2018.

[36] Y. Li, R. Mai, L. Lu, T. Lin, Y. Liu, and Z. He, "Analysis and transmitter currents decomposition based control for multiple overlapped transmitters based WPT systems considering cross couplings," *IEEE Trans. Power Electron.*, vol. 33, no. 2, pp. 1829–1842, Feb. 2018.

[37] Y. Li *et al.*, "Efficiency analysis and optimization control for input-parallel output-series wireless power transfer systems," *IEEE Trans. Power Electron.*, vol. 35, no. 1, pp. 1074–1085, Jan. 2020.

[38] C. Cheng, Z. Zhou, W. Li, Z. Deng, and C. C. Mi, "A power relay system with multiple loads using asymmetrical coil design," *IEEE Trans. Ind. Electron.*, vol. 68, no. 2, pp. 1188–1196, Feb. 2021.

[39] L. Wu, B. Zhang, and J. Zhou, "Efficiency improvement of the parity-time-symmetric wireless power transfer system for electric vehicle charging," *IEEE Trans. Power Electron.*, vol. 35, no. 11, pp. 12497–12508, Nov. 2020.

[40] Z. Yan *et al.*, "Efficiency improvement of wireless power transfer based on multitransmitter system," *IEEE Trans. Power Electron.*, vol. 35, no. 9, pp. 9011–9023, Sep. 2020.

[41] Z. Zhang, S. Zheng, Z. Yao, D. Xu, P. T. Krein, and H. Ma, "Analysis, design, and implementation of a spatially nested magnetic integration method for inductive power transfer systems," *IEEE Trans. Power Electron.*, vol. 36, no. 7, pp. 7537–7549, Jul. 2021.

[42] P. Tan, T. Peng, X. Gao, and B. Zhang, "Flexible combination and switching control for robust wireless power transfer system with hexagonal array coil," *IEEE Trans. Power Electron.*, vol. 36, no. 4, pp. 3868–3882, Apr. 2021.

[43] G. Ke, Q. Chen, L. Xu, X. Ren, and Z. Zhang, "Analysis and optimization of a double-sided S-*LCC* hybrid converter for high misalignment tolerance," *IEEE Trans. Ind. Electron.*, vol. 68, no. 6, pp. 4870–4881, Jun. 2021.

[44] V. Vu, D. Tran, and W. Choi, "Implementation of the constant current and constant voltage charge of inductive power transfer systems with the double-sided *LCC* compensation topology for electric vehicle battery charge applications," *IEEE Trans. Power Electron.*, vol. 33, no. 9, pp. 7398–7410, Sep. 2018.

[45] Y. Chen *et al.*, "Variable-parameter T-circuit-based IPT system charging battery with constant current or constant voltage output," *IEEE Trans. Power Electron.*, vol. 35, no. 2, pp. 1672–1684, Feb. 2020.

[46] D. Ahn, S. Kim, J. Moon, and I. Cho, "Wireless power transfer with automatic feedback control of load resistance transformation," *IEEE Trans. Power Electron.*, vol. 31, no. 11, pp. 7876–7886, Nov. 2016.

[47] G. Buja, M. Bertoluzzo, and K. N. Mude, "Design and experimentation of WPT charger for electric city car," *IEEE Trans. Ind. Electron.*, vol. 62, no. 12, pp. 7436–7447, Dec. 2015.

[48] X. Qu, H. Chu, S. Wong, and C. K. Tse, "An IPT battery charger with near unity power factor and load-independent constant output combating design constraints of input voltage and transformer parameters," *IEEE Trans. Power Electron.*, vol. 34, no. 8, pp. 7719–7727, Aug. 2019.

[49] R. Yue, C. Wang, H. Li, and Y. Liu, "Constant-voltage and constant-current output using P-C*LCL* compensation circuit for single-switch inductive power transfer," *IEEE Trans. Power Electron.*, vol. 36, no. 5, pp. 5181–5190, May 2021.

[50] Y. Li *et al.*, "Reconfigurable intermediate resonant circuit based WPT system with load-independent constant output current and voltage for charging battery," *IEEE Trans. Power Electron.*, vol. 34, no. 3, pp. 1988–1992, Mar. 2019.

[51] D. Wang, X. Qu, Y. Yao, and P. Yang, "Hybrid inductive-power-transfer battery chargers for electric vehicle onboard charging with configurable charging profile," *IEEE Trans. Intell. Transp. Syst.*, vol. 22, no. 1, pp. 592–599, Jan. 2021.

[52] Y. Chen, H. Zhang, S. Park, and D. Kim, "A switching hybrid *LCC*-S compensation topology for constant current/voltage EV wireless charging," *IEEE Access*, vol. 7, pp. 133924–133935, 2019.

Quanlei Zhang (Student Member, IEEE) was born in Suzhou, China, in 1996. He received the Graduate degree from the Liaoning University of Technology, Jinzhou, China, in 2019. He is currently working toward the M.S. degree in electrical engineering with Qingdao University, Qingdao, China.

His research interests include wireless power transfer.

Chunfang Wang (Member, IEEE) received the B.S. degree in automatic testing technology from Northeast Heavy Machinery College, Qiqihar, China, in 1984, the M.S. degree in power electronics and power drives from Tsinghua University, Beijing, China, in 1993, and the Ph.D. degree in electrical engineering from Xi'an Jiaotong University, Xi'an, China, in 2010.

From 1984 to 1990, he was a Research Assistant with Taiyuan Heavy Machinery College. Since 1993, he has been a Lecturer with the Department of Electrical Engineering, Qingdao University, Qingdao, China, where he is currently a Full Professor. His research interests include wireless power transfer technologies, electromagnetic and thermal field simulation of inductor devices, and small and medium-sized photovoltaic converters.

Hao Yuan (Student Member, IEEE) was born in Shanxi, China, in 1996. He received the Graduate degree from Shanxi University, Taiyuan, China, in 2019. He is currently working toward the M.S. degree in electrical engineering with Qingdao University, Qingdao, China.

His research interests include wireless power transfer.

Shuo Zhang (Student Member, IEEE) was born in Weifang, China, in 1997. He received the Graduate degree in 2019 from Qingdao University, Qingdao, China, where he is currently working toward the M.S. degree in electrical engineering.

His research interests include wireless power transfer.

Jingyu Wang (Student Member, IEEE) was born in Taian, China, in 1996. He received the Graduate degree from the Hefei University of Technology, Hefei, China, in 2019. He is currently working toward the M.S. degree in electrical engineering with Qingdao University, Qingdao, China.

His research interests include wireless power transfer.

Dongxue Li (Student Member, IEEE) was born in Dezhou, China, in 1997. She received the Graduate degree in 2019 from Qingdao University, Qingdao, China, where she is currently working toward the M.S. degree in electrical engineering.

Her research interests include wireless power transfer.

Lingyun Yang was born in Taiyuan, China, in 1999. He received the Graduate degree in 2021 from Qingdao University, Qingdao, China, where he is currently working toward the M.S. degree in electrical engineering.

His research interests include wireless power transfer.